



Single and binary nickel, copper, and zinc-based nanosized oxides as anode materials in lithium-ion batteries

Evren Egesoy^{1,2}, Özlem Kap^{3,4}, Fehmi Bardak¹, Nesrin Horzum^{3,*} , and Ahmet Ataç^{1,*}

¹ Department of Physics, Manisa Celal Bayar University, Yunusemre, Manisa, Turkey

² Central Research Laboratories Application and Research Center, Izmir Katip Çelebi University, Çiğli, Izmir, Turkey

³ Department of Engineering Sciences, Izmir Katip Çelebi University, Çiğli, Izmir, Turkey

⁴ Physics of Complex Fluids, MESA+ Institute for Nanotechnology, University of Twente, Enschede, Netherlands

Received: 17 August 2023

Accepted: 17 December 2023

© The Author(s), 2024

ABSTRACT

The demand for portable power sources with higher energy density and longer lifespan has prompted researchers to focus on developing better electrode materials for lithium-ion batteries (LIBs). Metal oxide nanoparticles have potential due to their low cost, high surface-area-to-volume ratio, strong reactivity, excellent size distribution, high theoretical capacities, and eco-friendly synthesis methods. However, there is still room for improvement in capacity retention and rate performance. To cope with this entail, the cycle performance of LIBs has been initially investigated utilizing single metal oxide anode materials including NiO, CuO, and ZnO nanostructures. Subsequently, binary oxides of Ni–Cu, Ni–Zn, and Cu–Zn have been synthesized to examine whether the binary structures boost the battery performance. NiCuO is the optimum anode material combining the benefits of NiO with the highest initial discharge capacity of 691 mAh g⁻¹ and the highest retention rate of CuO (49% after 30 cycles).

1 Introduction

Global energy consumption continues to rise, simultaneously with population and economic growth. The generation and storage of clean, safe, and green energy are technological and social issues that civilizations face as they grow and progress. As consumer demands increase, the trend toward more energy-dense sources increases, raising concerns about energy security. Natural gas, coal, oil, and other non-renewable fossil fuels are limited on the earth, and their replenishment

takes ages [1]. On the other hand, renewable energy sources are one of the most significant alternative energy sources because they can be produced repeatedly. To fulfill current energy demands and requirements, numerous research groups have been working diligently to build cutting-edge energy storage technology [2–4]. Batteries are particularly significant for continuous energy demands because of the high degree of uncertainty and irregular distribution of energy in other renewable energy sources found in nature. As a result, several battery types have been manufactured

Address correspondence to E-mail: nesrin.horzum.polat@ikc.edu.tr; ahmet.atac@cbu.edu.tr

and continue to be developed to meet the expanding need for energy.

Lithium-ion batteries (LIBs) are an attractive energy storage option for a variety of applications, including portable devices, electric automobiles, and hybrid electric vehicles. Even though LIBs have shown their commercial viability, several issues remain in terms of energy storage density, cycle life, and safety. In this regard, each component of LIBs should be improved tediously to meet desired characteristics. Graphite, commonly utilized as an anode material in battery technologies, has a theoretical specific capacity of 372 mAh g^{-1} , several safety concerns, and poor speed performance [5]. Interest in the use of transition metal oxides (MO_x , M: Co, Ni, Cu, Fe) as a possible anode material for improving the performance of LIBs has developed significantly [6]. By substituting transition metal oxides for the conventional lithium-ion progression mechanism, the specific capacity and high-rate performance of LIBs are increased during the charge/discharge process. Thus, utilizing the conversion reactions of metal oxides, high energy density, and capacity can be obtained. Among metal oxides, ZnO has a higher theoretical specific capacity (978 mAh g^{-1}) compared to NiO (718 mAh g^{-1}) and CuO (670 mAh g^{-1}) [7]. Contrary to the theoretical capacity, due to the fast volume expansion associated with the decrease in electrical conductivity, ZnO materials exhibit poor cycle stability and rate capability during lithium-ion transfer between the anode and cathode. In addition, the drastic volume change during the lithiation/delithiation process leads to rapid capacity reduction and low cycle stability. Because the inactive state of Li_2O leads to a decrease in electrical conductivity and structural stability during the process [8].

To overcome these issues, porous and/or nanosized metal oxides with various structures such as nanorods, nanosheets, nanotubes, and nanofibers have been developed for improving electrochemical performance [9–11]. Nanostructured metal oxide anode materials can be divided mainly into (i) insertion/intercalation (e.g., $\text{Li}_4\text{Ti}_5\text{O}_{12}$, NiVO_3), (ii) conversion (e.g., MO_x (M=Cr, Mn, Fe, Co, Ni, Cu, Zn, Mo, Ru)), and (iii) alloying-type (e.g., SiO_x , SnO_2 , GeO_2 , SbO) [12, 13].

A representative example was reported by Hernan and co-workers [14], who described the electrochemical characteristics of two-dimensional nanostructured NiO produced by calcination of $\beta\text{-Ni}(\text{OH})_2$. The

specific capacity of NiO nanoplatelets due to their mesoporous texture and microstructural properties was found to be higher than the theoretical capacity at moderate rates. On the other hand, Song et al. [7] stated that the microstructural changes caused by the amorphization of the crystalline surface oxide layer and the increase of the lattice defect density in the Ni struts during the lithiation process not significantly affect the good electrochemical performance of the material. The enhanced electrical conductivity and faster kinetics of Ni nanoparticle decorated ZnO nanorod anode had been reported by Park and co-workers [15]. Wang et al. [16] emphasized the synergistic effect of CuO nanowires (well-aligned core) and Co_3O_4 nanosheets (highly porous shell) as an anode material with good cycle performance, high reversible capacity, and excellent rate capability.

The electrodes produced from nanostructured metal oxides showed much higher capacities compared to graphite carbon [12]. However, the aggregation properties of nanoscale materials during the repeated discharge-charge process degrade the electrochemical properties (reversible capacity, cycle life, etc.) of nanomaterial electrodes. Moreover, the traditional electrode preparation procedure in which active materials and electronic conductive substances (usually carbon black) are embedded in the non-electroactive polymer matrix limit the kinetic process of nanomaterials. Consequently, the electrochemical performance of nanomaterials is highly dependent on fabrication methods [17]. To date, a variety of methods have been used including ball milling, wet chemical, pyrolysis, precipitation, atomic layer deposition, and electrospinning [18].

In this work, metal oxide nanoparticles were synthesized by the thermal decomposition of milled nickel, copper, and zinc salts. The anode performances of the single and binary metal oxide nanoparticles (NiO, CuO, ZnO, NiCuO, NiZnO, and CuZnO) for LIBs have been systematically investigated for the first time and associated with EIS and CV measurements. The optimum metal oxides are CuO and NiCuO which have capacity retention of 49% and 24% after 30 cycles, respectively. There is a strong correlation between the charge transfer resistance and the capacity of the battery. On the other hand, ZnO has rapid capacity fading, which is attributed to the irreversible electrochemical reaction.

2 Experimental

2.1 Synthesis of single and binary metal oxide nanoparticles

Single and binary metal oxide nanoparticles were synthesized by the direct thermal decomposition method. Nickel (II) acetate tetrahydrate ($\text{Ni}(\text{CH}_3\text{COO})_2 \cdot 4\text{H}_2\text{O}$, $\geq 99\%$), copper(II) nitrate hemi(pentahydrate) ($\text{Cu}(\text{NO}_3)_2 \cdot 2\frac{1}{2}\text{H}_2\text{O}$, 98%), and zinc(II) acetate dihydrate ($\text{Zn}(\text{CH}_3\text{COO})_2 \cdot 2\text{H}_2\text{O}$, $\geq 98\%$) were purchased from Sigma-Aldrich and Riedel Haën. The particle size of the metal precursors was reduced by a disc milling (Retsch-RS 200, Germany) at 1000 rpm for about 4 min. A 5 g of each metal salt or different combinations of mixed metal salts in a mol ratio of 1:1 were separately placed into the alumina crucibles and subsequently calcinated in a muffle oven (Protherm furnaces, PLF/20/27, Turkey). Based on the results of our previous study [19], the calcination parameter was selected as 400 °C and 5 h with a heating rate of 10 °C min^{-1} , and the mixtures were allowed to cool down to room temperature.

2.2 Characterization of the metal oxide nanoparticles

Thermogravimetric analysis (TGA) was performed using a TA Instruments SDT-Q600 under an oxygen atmosphere and heating rate of 10 °C min^{-1} . X-ray Diffractometer (XRD, Philips X'Pert Pro $\text{CuK}\alpha$) was used to determine the crystal structure of the samples. The sizes of the crystallites were estimated by the Scherrer equation [20]. The morphological characterization of the metal oxide nanoparticles was carried out by scanning electron microscopy (SEM) at accelerating voltages of 5–15 kV and working distances of 5–10 mm in a Carl Zeiss 300 VP. Energy-dispersive X-ray (EDX) analysis was also performed to determine the chemical composition of the nanoparticles. The diameter of the nanoparticles was statistically estimated from SEM micrographs by using the software Fiji/ImageJ. Brunauer-Emmet-Teller methodology (BET, Micrometrics 3Flex) was used to calculate the N_2 adsorption isotherm of the nanoparticles.

2.3 Electrochemical measurements

The materials containing hybrid and single nanostructures were used as active powders for electrode construction. The anode electrode was obtained by mixing the active powders, carbon black as a conductive material, and polyvinylidene difluoride (PVDF) binder in *N*-methyl-2-pyrrolidone (NMP) solvent in a ratio of 90:5:5 with a mixer mill. The slurry from the mixture was coated by a doctor blade on an aluminum foil current collector with a coating thickness of 200 μm . Then, the slurries covered on aluminum foil were kept on the hot plate for 2 h at 120 °C for pre-drying and cut into 18 mm diameter discs. They were dried under vacuum at 120 °C for 12 h to remove the solvent and moisture. Approximately, 13 mg cm^{-1} of active residual material was loaded on the electrode. In the next step, cells were formed in an argon-filled glove box using lithium foil as the counter electrode, 1 M LiPF_6 in (50:50) ethylene carbonate and diethyl carbonate (EC: DEC) solution as the electrolyte, and glass microfiber paper were used as a separator. Galvanostatic cycling with potential limitation (GCPL), cyclic voltammetry (CV), and electrochemical impedance spectroscopy (EIS) measurements were performed by a potentiostat/galvanostat (Bio-Logic Science Instruments, VMP-300). Galvanostatic cycling was carried out at different current densities (100, 200, and 400 mA g^{-1}) in the potential range of 0.001–3.0 V over 10 cycles. Cyclic voltammograms were recorded at the same potential ranges and at a scanning rate of 1 mV s^{-1} . EIS measurements were performed at room temperature with an amplitude of ± 10 mV AC and a frequency range of 100 kHz to 10 mHz. Equivalent circuit fitting of EIS data was obtained using EC-Lab Software V11.33.

3 Result and discussion

The preparation of single and binary metal oxide nanoparticles by milling and subsequent controlled thermal treatment using the precursors of environmentally friendly, cost-effective, and earth-abundant elements, namely Ni, Cu, and Zn is presented. Thermal, structural, and morphological characterizations of the NiO, CuO, ZnO, NiCuO, NiZnO, and CuZnO nanoparticles were performed and their performances

as anode electrodes in lithium-ion batteries were comparatively evaluated.

The conditions used to prepare metal oxides have a significant impact on their properties, such as specific surface area, porosity, crystallinity, phase composition, particle size, and thus performances in various fields of application. Important criteria include the type of precursor materials, heat treatment (temperature, time, and heating/cooling rate), and the nature of the surrounding atmosphere. Metal acetate and nitrate hydrates are often preferred as precursors to metal oxides, as they can be readily converted to their oxide form by thermal or oxidative degradation [21, 22]. In the first instance, TGA was performed to determine the metal oxide content in the resulting material. Figure 1 shows the TGA curves of both single and binary metal oxide nanoparticles. The rapid weight loss at the temperature of 100 °C resulted from the evaporation of physically adsorbed hydrated water molecules of the metal precursors. The weight loss in the range of 250 to 400 °C is due to the decomposition of metal salts into metal oxides. The single metal precursors showed total weight losses of 76, 70, and 79% for Ni, Cu, and Zn salts, respectively (Fig. 1a). The observed weight losses from the TGA curve are lower than the calculated theoretical value, assuming all the metal salts are converted to oxide forms. The decrement might be explained by the sublimation of metal acetate/nitrate species, hydrolysis of surface acetate groups, and formation of acetic acid/nitric acid to the gas phase or the formation of other volatile metal-organic compositions

[23–25]. The order of increasing thermal stability of the single oxides is ZnO < CuO < NiO. Furthermore, the stability of the single oxides was enhanced when using two metal precursors (Fig. 1b). Zn and Cu precursors showed improvement in their thermal properties when mixed with other precursors. On the other hand, while the addition of Cu to Ni improved its thermal properties, Zn did not change its thermal stability. The correlation between the thermal stability and melting points of transition metal oxides has been attributed to the electronic structure of the elements [26]. After 400 °C, no further weight loss has been observed up to 700 °C, indicating the formation of CuO/NiO (~26%), NiO/ZnO (~32%), and CuO/ZnO (~35%) composite nanoparticles.

The XRD patterns of metal oxide nanoparticles are depicted in Fig. 2. For the single metal oxides, the reflections can be indexed to cubic NiO, monoclinic CuO, and hexagonal ZnO with 79, 82, and 70% agreement, respectively, in Fig. 2(left). The patterns in Fig. 2(right) correspond to the cubic NiCuO, hexagonal NiZnO and CuZnO for the binary metal oxides with 62, 76, and 70% agreement, respectively. Although more than 50% belongs to binary metal oxides, they contain small amounts of single metal oxides forming the binary compound. A lesser amount of single oxides was observed for NiZnO and CuZnO compared to NiCuO. The radius of Zn²⁺ ions is similar to that of Cu²⁺, however they have higher ionic radii than Ni²⁺ ions, indicating that Ni ions have successfully filled the ZnO or CuO lattice [27].

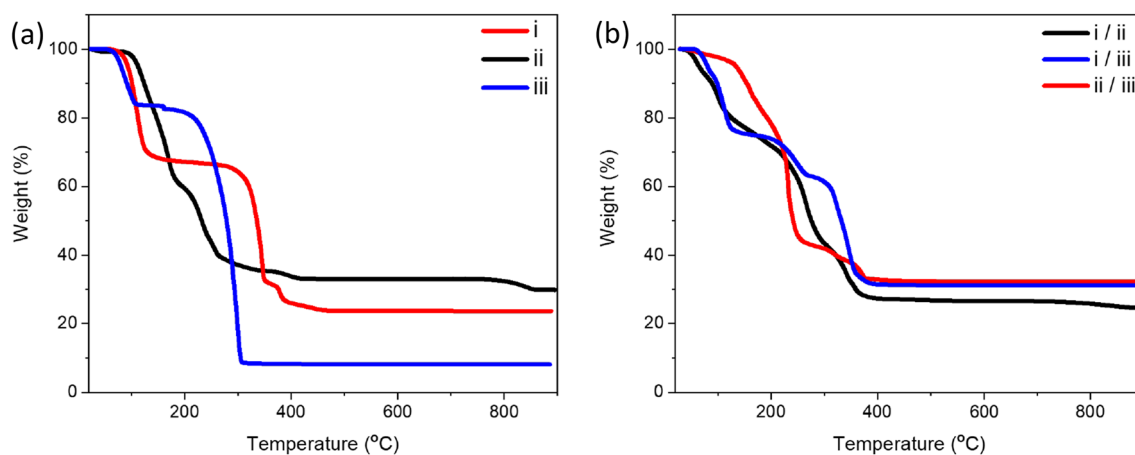


Fig. 1 TGA curve of the metal precursors **a** Ni(CH₃COO)₂·4H₂O(i), Cu(NO₃)₂·2.5H₂O(ii), Zn(CH₃COO)₂·2H₂O(iii), **b** Ni(CH₃COO)₂·4H₂O/Cu(NO₃)₂·2.5H₂O(i/ii), Ni(CH₃COO)₂·4H₂O/

Zn(CH₃COO)₂·2H₂O(i/iii), Cu(NO₃)₂·2.5H₂O/Zn(CH₃COO)₂·2H₂O(ii/iii)

Fig. 2 XRD patterns of the single (left) and binary (right) metal oxide nanoparticles

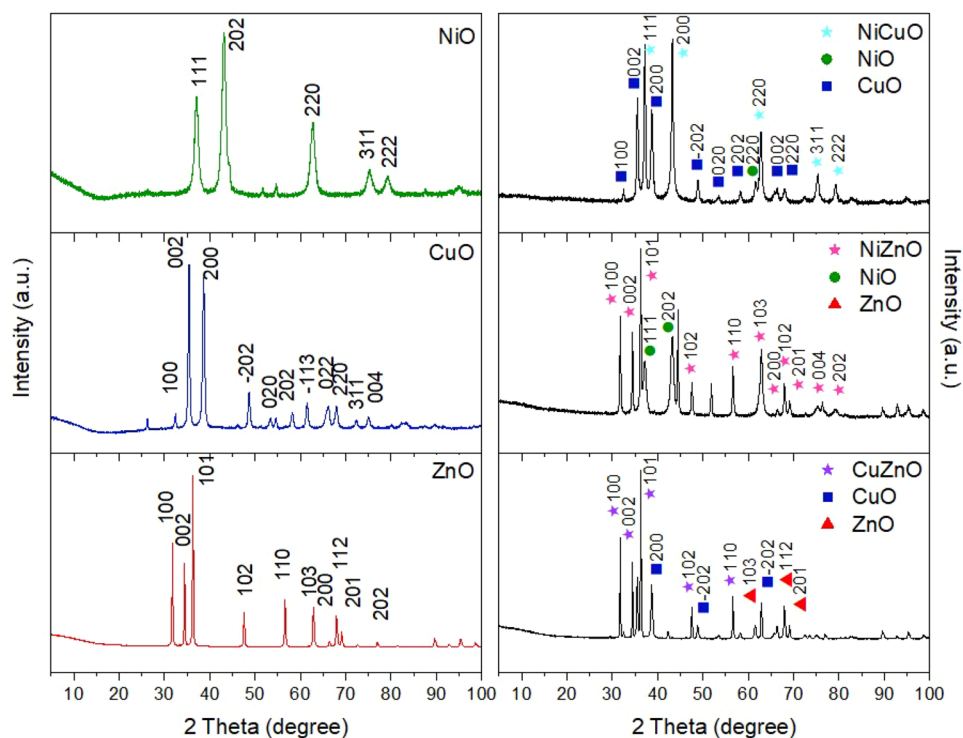


Table 1 Average particle size and crystallite size of the metal oxide nanoparticles

Metal oxide nanoparticles	Crystallite Size* (nm)	Particle Size** (nm)
NiO	15.04	850 ± 80
CuO	16.21	The nanosheets (~300 nm in length and ~80 nm in width) On the inner structure of the Microparticles (2.0 ± 0.3 μm)
ZnO	30.36	145 ± 12
NiCuO	32.18	96 ± 6
NiZnO	18.33	248 ± 17
CuZnO	17.32	63 ± 7

*Obtained from XRD patterns using Scherrer equation

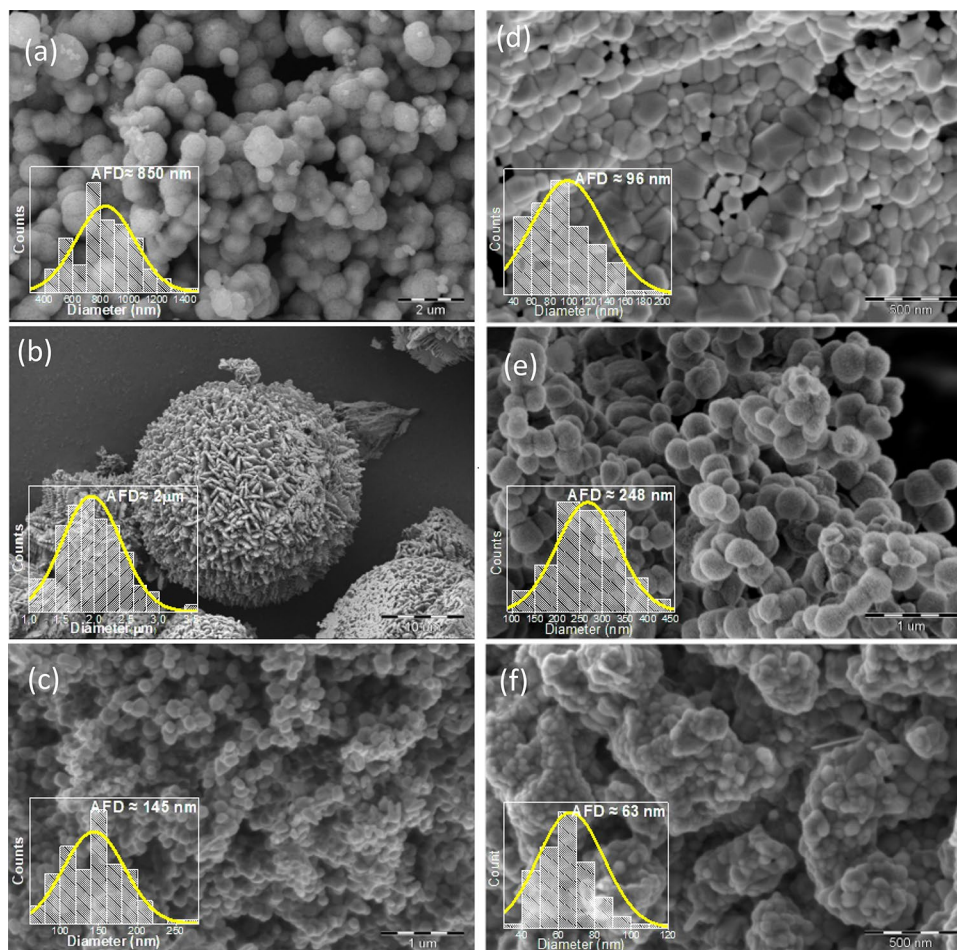
** From SEM images using Image J software

The average crystallite size and particle size of the metal oxide nanoparticles are listed in Table 1. Using the Scherrer equation, the crystallite sizes calculated are in the range of 15–18 nm, except ZnO and NiCuO (30–32 nm). Although the crystal structures of NiZnO and CuZnO are identical to that of ZnO, their crystallite sizes were reduced.

The morphology of the single and binary metal oxide nanoparticles was characterized by SEM. Figure 3a–c displays the micrographs and diameter distributions of the single metal salts after calcination.

The larger-sized CuO microparticles with internal nanostructures from nitrate decomposition, whereas smaller-sized NiO and ZnO nanoparticles from acetate decomposition were obtained (Table 1). This might be explained by the thermal degradation of Cu nitrate salt at lower temperatures than Ni and Zn acetate salts. Thus, further increases above the decomposition temperature resulted in larger particles. Wang et al. [28] also examined the effect of copper precursors on the morphology of the CuO structures. The CuO size was reduced when the copper source changed from copper nitrate to copper acetate. The decreasing trend was attributed to the acid radical ions (nitrate is an inorganic strong acid radical and acetate is an organic weak acid radical) having an effect on the nucleation and growth of the copper precursors. On the other hand, NiO and ZnO spherical nanoparticles revealed smooth surfaces. Although CuO microparticles are also spherical, the size and surface morphology are rather different from NiO and ZnO. The CuO spheres are composed of nanosheets and the width is approximately a quarter of its length.

Fig. 3 SEM micrographs of the metal oxide nanoparticles **a** NiO, **b** CuO, **c** ZnO, **d** NiCuO, **e** NiZnO, and **f** CuZnO



Liu and Zeng [29] synthesized CuO microparticles at 100 °C with similar morphology which they called dandelion-like. The dandelion-like CuO structures were formed by the self-assembly and Ostwald ripening mechanism. In addition, the effect of ammonia amount, source of copper, and reaction time on the morphology of the CuO structures were verified [28].

Although the hydrothermal method has the advantage of obtaining metal oxide nanostructures at low temperatures, metal oxide nanostructures can be obtained in a single step by simply milling the metal precursors before thermal decomposition. Figure 3d–f shows the micrographs of binary metal oxide nanoparticles. The binary oxides of Ni had lower particle sizes compared to their single oxides. Analogously, Cu reduced the particle size of NiCuO and CuZnO while changing their shapes into agglomerated shapeless particles. EDX patterns of the single and binary metal oxide particles showed only related metal and oxygen, and the atomic compositions of metals contain more than 50% of the total components, confirming

Table 2 Surface area characteristics of the metal oxide nanoparticles

Metal oxide nanoparticles	BET specific surface area (m ² g ⁻¹)	Pore volume (cm ³ g ⁻¹)
NiO	60.6025	0.069427
CuO	1.182	0.002384
ZnO	5.7757	0.012834
NiCuO	5.4097	0.01175
NiZnO	20.5334	0.036978
CuZnO	0.2545	0.000517

the formation of metal oxides with oxygen (Figs. S1 and S2). Table 2 gives the values of surface area and pore volume. The lower specific surface area and pore volume of synthesized metal oxide nanoparticles are consistent with the formation of aggregated particles with less accessible surface area. Except for CuZnO, hysteresis loops in the nitrogen adsorption and desorption isotherms (Fig. S3) belong to type IV

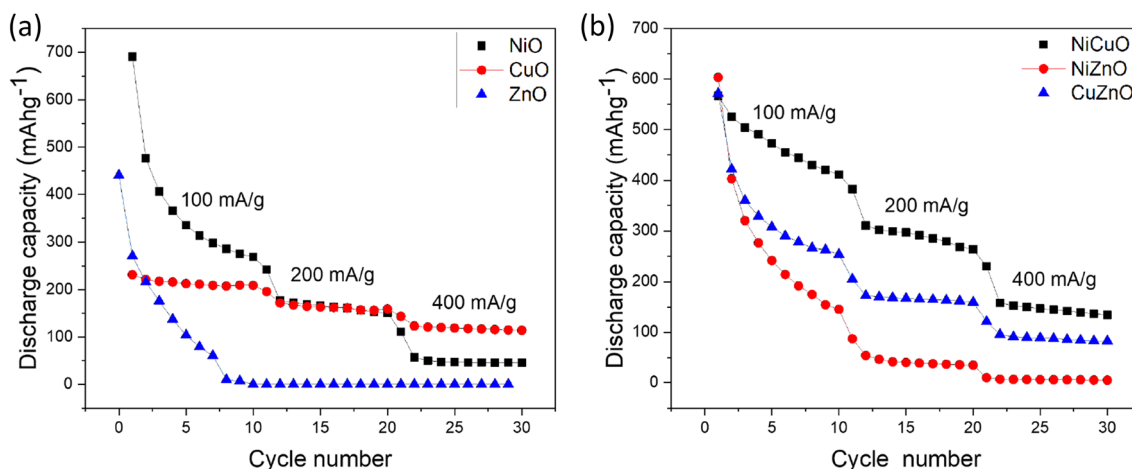


Fig. 4 Cyclic specific discharge capacity of the nanoparticles **a** single metal oxides, **b** binary metal oxides

as classified by IUPAC [30], which indicates the presence of mesopores.

Figure 4a shows the cycle performance of the single NiO, CuO, and ZnO metal oxides nanoparticles anode electrodes at 100, 200, and 400 mA g⁻¹ discharge rates in the voltage change range of 0.01–3 V. The initial discharge capacities of NiO, CuO, and ZnO nanoparticles were 691, 233, and 441 mAh g⁻¹. The discharge capacity of NiO dropped to 267 mAh g⁻¹ at 100 mA g⁻¹, to 151 mAh g⁻¹ at 200 mA g⁻¹, and 46 mAh g⁻¹ at 400 mA g⁻¹ after 10 cycles for each discharge rate. Although the initial discharge capacity of NiO was the highest compared to CuO and ZnO, its capacity retention was poor, which ran into an amount equivalent to 7%. On the other hand, for CuO nanoparticles, the initial capacity was lower with a discharge capacity of 233 mAh g⁻¹. However, capacity retention was the highest with 49% after 30 cycles.

ZnO had an initial discharge capacity of 441 mAh g⁻¹, and after the first 10 cycles at 100 mA g⁻¹, the capacity loss was 99%. The ZnO nanoparticles lost the electrode activity after 30 cycles. Ultimately, the order of increasing the initial discharge capacity of the single oxides is CuO < ZnO < NiO while the retention rate order after 30 cycles is ZnO < NiO < CuO. Figure 4b shows the discharge capacity of the binary metal oxide anode materials over 30 cycles. It can be seen that the initial discharge capacities of NiCuO, NiZnO, and CuZnO materials were nearly similar with 567, 604, and 572 mAh g⁻¹, respectively. After the ten cycles, the capacity of NiZnO and CuZnO decreases by 76% and 56% at 100 mA g⁻¹, and at 200 mA g⁻¹ discharge rate, the capacity loss reached 94% and 72%, respectively. There

was no capacity fading after 30 cycles, and the capacity retention was 1% for NiZnO and 14% for CuZnO. In binary oxides, the initial discharge capacity varies inversely with the retention rate after 30 cycles, i.e., NiCuO with the lowest capacity has the highest retention rate. The advantage of the binary metal oxides can be considered as; first, the initial capacity increase compared to single metal oxides counterparts; second, an obvious capacity boost in the Li-ion battery. While the capacity fade was observed for the single nanoparticle ZnO anode material, its binary products with CuO and NiO provided a capacity increase. However, CuZnO and NiZnO capacity retentions were lower than the single nanoparticles of CuO and NiO due to the low capacity performance of ZnO. In comparison to ZnO, the NiCuO anode material, which is a binary product of CuO and NiO, enhanced its capacity after 30 cycles due to the synergistic effect. NiCuO retained 73% of its capacity after the first 10 cycles, 46% after 20 cycles, and 24% after the last 30 cycles. Although NiCuO has lower capacity retention than CuO, its discharge capacity is 2.5 times greater after 30 cycles. This demonstrates that the binary products preserve the capacity features of single metal oxide nanoparticles and that the synergistic effect of the high-performance anode materials is achieved.

The limiting factors for the battery capacity are the particle size and distribution, particle shape, surface area, crystallinity or amorphous structure. The better capacity retention of CuO can be attributed to the secondary nanosheets on the inner structure of microparticles with interspacing to accommodate and restrain the volume changes occurring during cycling (see

Fig. 3b) [31]. Furthermore, the densely linked NiCuO and CuZnO nanoparticles (see Fig. 3d and f) might have slow electrolyte diffusion and a lower effective contact area, after the charge-discharge process [32]. This is mainly due to the more stable structure during the cycling of the binary oxides with the coating layer, which can protect the particle from the side reactions on the surface [33]. The larger surface area of the materials affects the battery performance negatively. A fast surface degradation takes place which potentially may lead to accelerated consumption of the lithium ions, resulting in rapid impedance growth [34]. Although NiO nanoparticles have a larger surface area compared to CuO nanoparticles, they have a high initial capacity but a poor cycling capacity. On the other hand, the inevitable capacity fading of ZnO due to its low conductivity hence poor kinetics and high-volume expansion during electrochemical charging-discharging is a well-known issue. The pulverization and aggregation of the Zn clusters can also be attributed to the loss of capacity [31, 35]. Therefore, the binary oxides of Zn, i.e., CuZnO and NiZnO, are likely to have poor performance.

The metal oxide anode cells were charged and discharged at 100, 200, and 400 mA g⁻¹ current loads at room temperature in the voltage window of 0.01–3 V. The specific capacity and current load were calculated based on the total mass of the anode material. In Fig. 5, the profiles exhibit non-identical charge-discharge cycles. CuO anode cell initial discharge and charge capacities are 224 mAh g⁻¹ and 226 mAh g⁻¹, respectively. NiO, the second promising material, has the highest initial discharge capacity at 691 mAh g⁻¹ and the highest initial charge capacity at 476 mAh g⁻¹. However, according to the results of the charge/discharge experiments, the capacity retention of the CuO anode cell is 63%, whereas the NiO cell only has 16%. In addition, the ZnO cell had very poor capacity retention; the capacity faded significantly after being charged with a 100 mA g⁻¹ current load. The capacity retention of CuNiO and CuZnO has not diminished similarly to that of NiZnO. CuNiO has a better charge/discharge performance than CuZnO, with a capacity retention of 41%. This result demonstrates that improved capacity performance can be obtained for NiO nanoparticles by

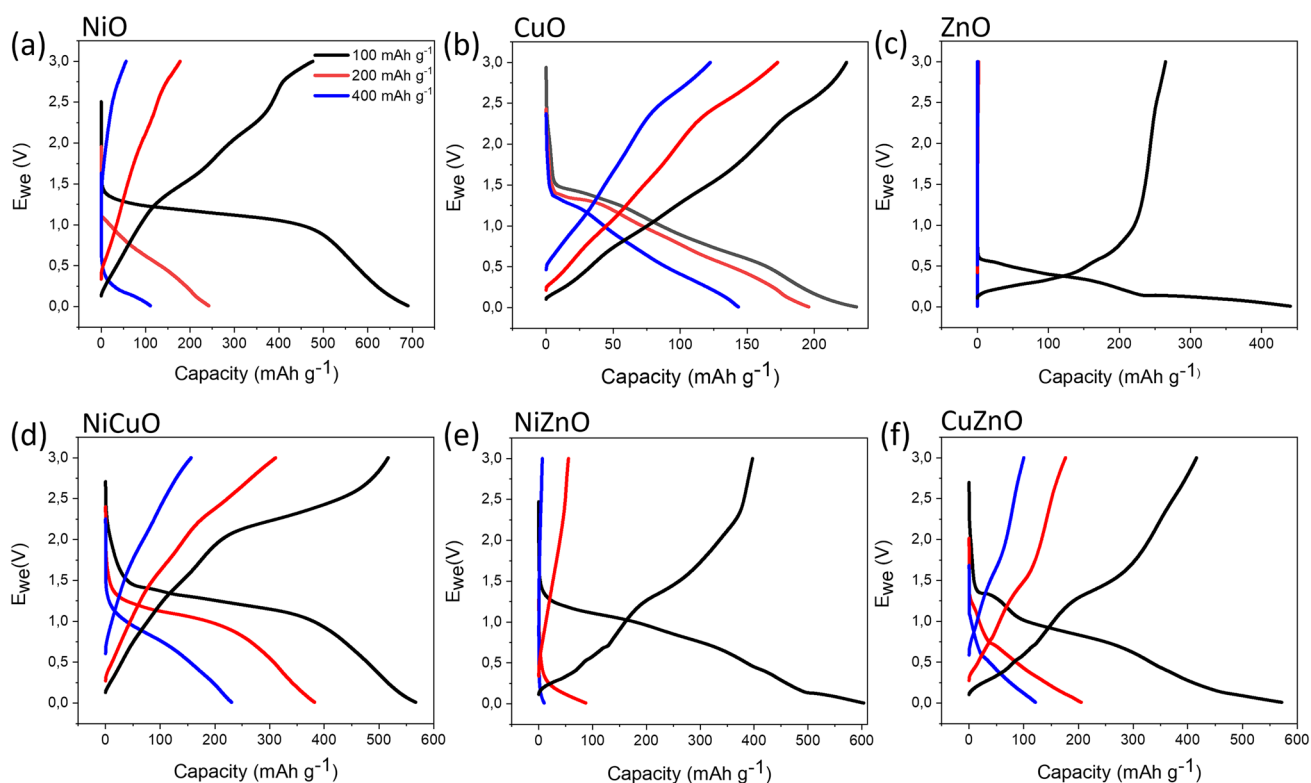


Fig. 5 Charge-discharge profiles of the **a** CuO, **b** NiO, **c** ZnO, **d** NiCuO, **e** CuZnO, and **f** NiZnO cells at 100, 200, 400 mA g⁻¹ over the voltage range of 0.01–3 V

fabricating them with CuO nanoparticles in a binary mixture.

The battery impedance measurements have been performed before and after charge/discharge cycles by electrochemical impedance spectroscopy (EIS) which is a highly effective non-destructive in-situ method. The EIS spectra of the single and binary metal oxide nanoparticles are shown in Fig. 6. The Nyquist plots were obtained in the range of 10 mHz–100 kHz before the charge and discharge process after 10 and 30 charge/discharge cycles for each metal oxide anode material as seen in Fig. 6a–f. The high- and mid-frequency regions of the EIS curves are detailed in Fig. S4. The data were fitted with EC-Lab software to determine the equivalent circuit elements by using the two models in Fig. 7a and b for anode materials before the cell preparation and after 10 and 30 charge/discharge cycles of the battery, respectively. The impedance data can provide information about the cell resistance of bulk material (R_s) in high-frequency regions (100 kHz–10 kHz), the solid interface layer between the electrode and electrolyte (R_{sei}), and charge transfer resistance (R_{ct}) in high- or mid-frequency regions (10

kHz–1 kHz). The constant phase elements (CPE) are employed to compensate non-ideal capacitor behavior of the double layer [36]. Moreover, the lithium diffusion process emerged Warburg diffusion resistance as a straight line at low-frequency region (1 kHz–10 mHz). In Fig. 6, EIS results showed a single semicircle prior to the charge and discharge cycles for each of the six metal oxides anode materials. The values of R_s and R_{ct} were obtained, but the Warburg impedance in the low-frequency region was omitted from this evaluation. The fitting results were shown in Fig. 7a–c for R_s , R_{sei} , and R_{ct} , respectively. CuO exhibited a relatively low internal resistivity compared to the other single and binary metal oxide nanoparticles. After 10 and 30 cycles, except for ZnO, the metal oxides showed a slight increase. This can occur as a result of electrolyte depletion and the development of microcracks in the particles [37]. Since there is no electrochemical reaction between the anode and the cathode before charge-discharge cycles, there is no solid electrolyte interphase layer (SEI). R_{ct} is related to the electrochemical reaction's kinetics and is affected by the surface coating, phase transition, bandgap structure, and particle size

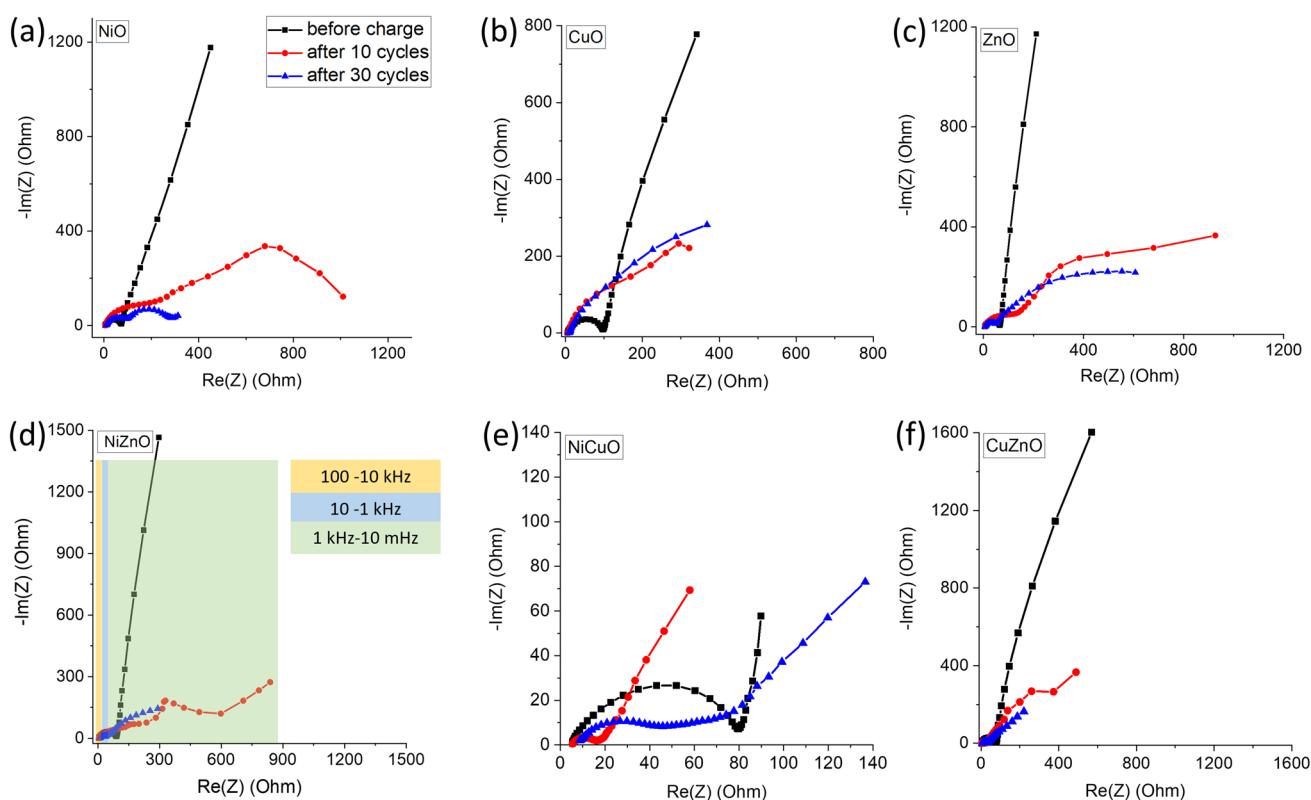


Fig. 6 EIS curves of the nanoparticles **a–c** single metal oxides and **d–f** binary metal oxide. In the plot of NiZnO, high-, mid-, and low-frequency regions are color-coded to show the corresponding frequency ranges

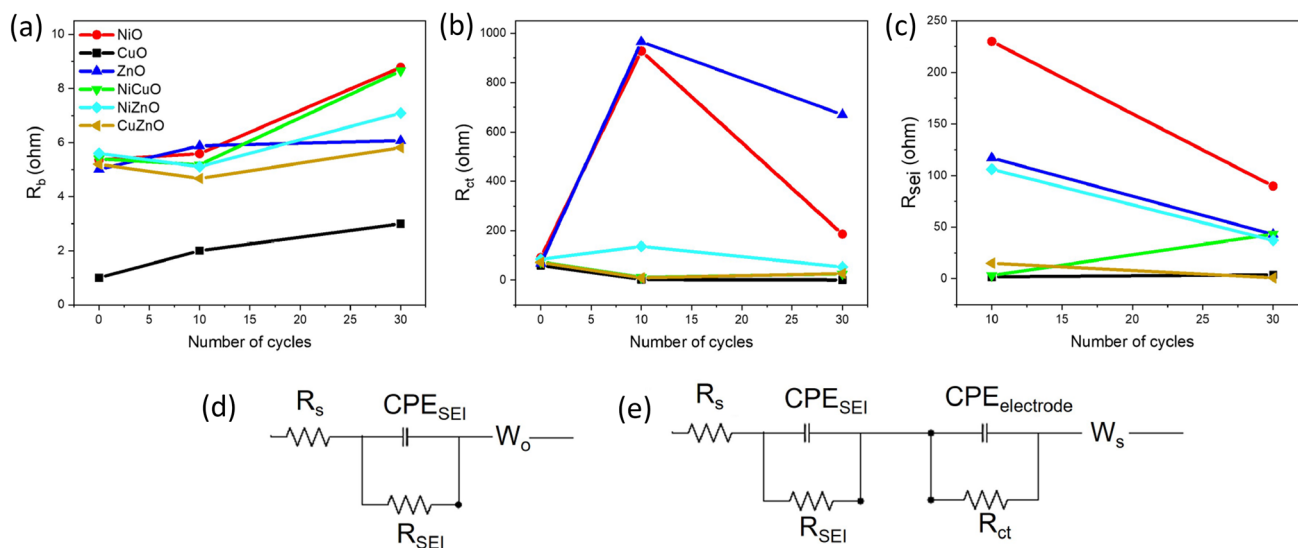


Fig. 7 The resistance fit values for R_s , R_{ct} prior to charge/discharge and for R_s , R_{sei} , R_{ct} **b** after 10 cycles and **c** after 30 cycles are based on the equivalent circuit model for six different metal oxide anode materials. Respective equivalent circuits applied

metal oxides nanoparticles **d** before and **e** after the charge/discharge cycles (The lines in the figure are guided for the visual observation)

[37]. Before the cycles, the surface area of the particle has a significant influence in the materials on the charge resistance property. Because, BET analysis revealed that NiO and NiZnO with very large particle sizes had the greatest R_{ct} , prior to the cell preparation. Following the charge/discharge cycles, the discharge capacities of the metal oxide anode materials were compared with the R_{ct} values. ZnO, which has the highest R_{ct} , suffered from capacity fading after 10 cycles. The total capacity loss values for ZnO, NiZnO, NiO, CuZnO, and NiCuO were 100, 94, 78, 72, and 54%, respectively, whereas the R_{ct} values decreased with the order of ZnO, NiO, NiZnO, CuZnO, and NiCuO with a good correlation with capacity measurements after 10 and 30 cycles. Due to the chemical reaction between the electrodes and electrolyte, a passivation layer forms on the anode surface, resulting in capacity loss and increased R_{sei} in the battery [38]. The change of R_{sei} between the 10th and 30th cycles was nearly constant for CuO and CuZnO and increased slightly for NiCuO. The capacity loss was 51, 85, and 76% for CuO, CuZnO, and NiCuO after 30 cycles, respectively. However, the R_{sei} of NiO, ZnO, and NiZnO were decreased, with a total capacity loss of 93, 100, and 99%, respectively, after 30 cycles. As a result, a decrease in R_{sei} can be linked to a greater capacity loss. Moreover, the reduction in capacitance can be attributed to the increase in the layer thickness while

the resistance decreases for NiO, ZnO, and NiZnO. Despite the relatively large pore size and surface area, the low capacity retention properties of NiO, ZnO, and NiZnO can only be explained by their electronic conductivity properties.

CV curves are shown in Fig. 8 for metal oxide nanoparticles at a scan rate of 1 mV/s. To investigate the electrochemical mechanism, the CV curves were tested throughout a voltage spectrum ranging from 0 to 3 V (vs Li/Li⁺). Figure 8a shows the CV tests for the single metal oxide nanoparticles. During the cathodic sweep, the reduction peaks for the NiO nanoparticles electrodes appear at 0.69 and 0.95 V. The strong peak at 0.69 V can be related to the reduction of NiO to Ni and is caused by the formation of amorphous Li₂O as well as the electrolyte decomposition that leads to the formation of the SEI layer [39, 40]. The anodic sweep for NiO nanoparticles includes two reductive peaks at 1.70 and 2.34 V, which correspond to the deformation of the SEI and Li₂O, and oxidation of Ni to Ni²⁺, respectively [41]. The broad cathodic peak at 0.7 V for CuO nanoparticles can be attributed to SEI formation [42]. During the anodic sweep, two oxidative peaks appeared at 2.00 and 2.55 V, which can be associated with the deformation of SEI film, oxidation of Cu to Cu₂O and CuO [43]. ZnO nanoparticles exhibit two anodic peaks at 0.64 and 1.63 V. The oxidation peak can be attributed to the Li⁺ storage in ZnO at 0.64 V,

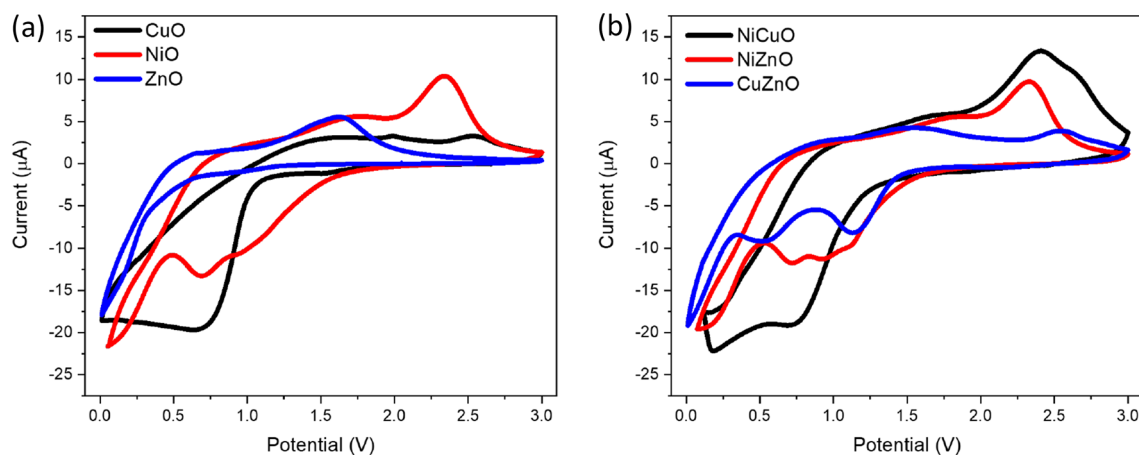


Fig. 8 CV curves of the **a** single metal oxides and **b** binary metal oxides

and the latter can be attributed to the oxidation to ZnO [44, 45]. However, there are no corresponding reduction peaks for those oxidation potential peaks. Therefore, the rapid capacity fading of the ZnO material can be explained due to the irreversible electrochemical reaction. Moreover, Pelliccione et al. [46] proposed two mechanisms to explain the capacity fading of ZnO anode material. The extended X-ray absorption fine structure results show that oxygen atoms are not positioned close to Zn atoms. First, this result can be explained by the growing size of the Zn particles within the Li_2O matrix after the battery charge/discharge cycles. Therefore, the results support that the loss of electrical contact occurs due to the cracking and fracturing of growing ZnO particles. The second mechanism is explained by the thickness of the Li_2O layers which form between the nanoparticles. Figure 8b shows the CV tests for the hybrid nanoparticles. The obtained oxidative and reductive peaks are shifted compared to the single nanoparticles. The binary mixtures of the particles exhibit reversible oxidation and reduction potential peaks. This feature can be caused to the enhanced cycle capacity of the metal oxide anode materials.

4 Conclusion

We have conducted a comprehensive investigation on the electrochemical anode performance of single and binary metal oxide nanoparticles in the context of their application in Li-ion batteries. The utilization of binary nanostructures has been found to enhance

battery performance, while the combination of these materials reduces their charge transfer resistance. Among the single nanoparticles, NiO and CuO exhibit higher capacity retention, whereas NiCuO demonstrates the highest capacity performance. Conversely, the binary compounds containing ZnO metal oxide nanoparticles exhibit lower battery performance. A comparison between NiO single nanoparticles and NiZnO binary nanoparticles reveals the detrimental effect of ZnO on performance. The capacity fading of ZnO material is attributed to irreversible electrochemical reactions observed during cyclic voltammetry (CV) scanning. The performance of lithium-ion batteries is influenced by various factors, including chemical composition, crystallinity, size, shape, and surface characteristics such as surface area, charge, and energy. However, it is evident that the dominance of charge transport resistance plays a crucial role in determining the overall performance of batteries.

Acknowledgements

This research was supported by the Scientific Research Projects Coordination Unit of Manisa Celal Bayar University (Project no. 2021-009). The authors thank Izmir Katip Çelebi University Central Research Laboratory for materials characterization. Prof. M. Kadri Aydınol, Energy Storage Devices and Battery Laboratory coordinator at Middle East Technical University is acknowledged for battery performance tests. Dr. Jannis Schlicke is also acknowledged for his

valuable comments about electrochemical impedance spectroscopy.

Author contributions

EE: Investigation, methodology, software, Writing—Original draft preparation. ÖK: Conceptualization of this study, methodology, software, Writing—Original draft preparation. FB: Resources, Writing—review & editing. NH: Conceptualization of this study, resources, Writing—Original draft preparation, Writing—review & editing. AA: Supervision, resources, Writing—review & editing

Funding

Open access funding provided by the Scientific and Technological Research Council of Türkiye (TÜBİTAK). This work was supported by Manisa Celal Bayar Üniversitesi (Grant No: 2021-009).

Data availability

All data generated or analyzed during this study are included in this manuscript.

Declarations

Competing interest The authors declare that they have no known competing financial interests or personal relationships that could have appeared to influence the work reported in this paper.

Supplementary Information The online version contains supplementary material available at <https://doi.org/10.1007/s10854-023-11838-0>.

Open Access This article is licensed under a Creative Commons Attribution 4.0 International License, which permits use, sharing, adaptation, distribution and reproduction in any medium or format, as long

as you give appropriate credit to the original author(s) and the source, provide a link to the Creative Commons licence, and indicate if changes were made. The images or other third party material in this article are included in the article's Creative Commons licence, unless indicated otherwise in a credit line to the material. If material is not included in the article's Creative Commons licence and your intended use is not permitted by statutory regulation or exceeds the permitted use, you will need to obtain permission directly from the copyright holder. To view a copy of this licence, visit <http://creativecommons.org/licenses/by/4.0/>.

References

1. W. Ernst, Sustainable energy and mineral resource extraction and consumption-can a viable biosphere be preserved?, in: *Mining, Society, and a Sustainable World* (Springer, 2009), pp. 125–149
2. B. Scrosati, J. Garche, Lithium batteries: status, prospects, and future. *J. Power Sources* **195**, 2419–2430 (2010)
3. D. Larcher, J.-M. Tarascon, Towards greener and more sustainable batteries for electrical energy storage. *Nat. Chem.* **7**, 19–29 (2015)
4. Ö. Kap, N. Horzum, C. Varlikli, *Hybridized nanomaterials for enhancing photocatalytic activity in solar fuel production, green photocatalytic semiconductors: recent advances and applications* (2022), pp. 817–861
5. Y. Sun, Q. Wu, G. Shi, Graphene based new energy materials. *Energy Environ. Sci.* **4**, 1113–1132 (2011)
6. C. Yuan, H.B. Wu, Y. Xie, X.W. Lou, Mixed transition-metal oxides: design, synthesis, and energy-related applications. *Angew. Chem. Int. Ed.* **53**, 1488–1504 (2014)
7. Y. Song, J. Hwang, S. Lee, B. Thirumalraj, J.-H. Kim, P. Jenei, J. Gubicza, H. Choe, Synthesis of a high-capacity NiO/Ni foam anode for advanced lithium-ion batteries. *Adv. Eng. Mater.* **22**, 2000351 (2020)
8. J. Theerthagiri, S. Salla, R. Senthil, P. Nithyadharseni, A. Madankumar, P. Arunachalam, T. Maiyalagan, H.-S. Kim, A review on ZnO nanostructured materials: energy, environmental and biological applications. *Nanotechnology* **30**, 392001 (2019)
9. V.K.H. Bui, T.N. Pham, J. Hur, Y.-C. Lee, Review of ZnO binary and ternary composite anodes for lithium-ion batteries. *Nanomaterials* **11**, 2001 (2021)
10. Ö. Kap, A. Inan, M. Er, N. Horzum, Li-ion battery cathode performance from the electrospun binary LiCoO₂ to ternary

- Li₂CoTi₃O₈. *J. Mater. Sci.: Mater. Electron.* **31**, 8394–8402 (2020)
11. L. Ji, Z. Lin, M. Alcoutlabi, X. Zhang, Recent developments in nanostructured anode materials for rechargeable lithium-ion batteries. *Energy Environ. Sci.* **4**, 2682–2699 (2011)
 12. P. Poizot, S. Laruelle, S. Grugeon, L. Dupont, J. Tarascon, Nano-sized transition-metal oxides as negative-electrode materials for lithium-ion batteries. *Nature* **407**, 496–499 (2000)
 13. H. Chang, Y.-R. Wu, X. Han, T.-F. Yi, Recent developments in advanced anode materials for lithium-ion batteries. *Energy Mater.* **1**, 24 (2021)
 14. A. Caballero, L. Hernán, J. Morales, Z. González, A. Sánchez-Herencia, B. Ferrari, A high-capacity anode for lithium batteries consisting of mesoporous NiO nanoplatelets. *Energy Fuels* **27**, 5545–5551 (2013)
 15. H.N. Park, S.H. Park, J.H. Shin, S.-H. Jeong, J.Y. Song, Template-free electrochemical growth of Ni-decorated ZnO nanorod array: application to an anode of lithium ion battery. *Front. Chem.* 415 (2019)
 16. J. Wang, Q. Zhang, X. Li, D. Xu, Z. Wang, H. Guo, K. Zhang, Three-dimensional hierarchical Co₃O₄/CuO nanowire heterostructure arrays on nickel foam for high-performance lithium ion batteries. *Nano Energy* **6**, 19–26 (2014)
 17. Q. Pan, H. Jin, H. Wang, G. Yin, Flower-like CuO film-electrode for lithium ion batteries and the effect of surface morphology on electrochemical performance. *Electrochim. Acta* **53**, 951–956 (2007)
 18. S. Fang, D. Bresser, S. Passerini, Transition metal oxide anodes for electrochemical energy storage in lithium-and sodium-ion batteries. *Adv. Energy Mater.* 1902485 (2020)
 19. M. Tetik, O. Kap, G. Dutta, V. Kilic, D. Moschou, N. Horzum, An enzyme-free glucose biosensor based on CuO nanostructures anchored on flexible printed circuit board, in: 3rd International Eurasian Conference on Biological and Chemical Sciences (EurasianBioChem 2020) (2020)
 20. J.I. Langford, A. Wilson, Scherrer after sixty years: a survey and some new results in the determination of crystallite size. *J. Appl. Crystallogr.* **11**, 102–113 (1978)
 21. J.-G. Yoon, T.K. Song, Fabrication and characterization of ferroelectric oxide thin films, in: *Handbook of Thin Films* (Elsevier, 2002), pp. 309–367
 22. N. Horzum, M.E. Hilal, T. Isik, Enhanced bactericidal and photocatalytic activities of ZnO nanostructures by changing the cooling route. *New J. Chem.* **42**, 11831–11838 (2018)
 23. J.C. De Jesus, I. González, A. Quevedo, T. Puerta, Thermal decomposition of nickel acetate tetrahydrate: an integrated study by TGA, QMS, and XPS techniques. *J. Mol. Catal. A: Chem.* **228**, 283–291 (2005)
 24. C.-C. Lin, Y.-Y. Li, Synthesis of ZnO nanowires by thermal decomposition of zinc acetate dihydrate. *Mater. Chem. Phys.* **113**, 334–337 (2009)
 25. B. Małecka, A. Łącz, E. Drożdż, A. Małcki, Thermal decomposition of d-metal nitrates supported on alumina. *J. Therm. Anal. Calorim.* **119**, 1053–1061 (2015)
 26. Y.S. Malakhov, G. Samsonov, Regularities governing the thermal stability of oxides of the transition metals, *Soviet. Powder Metall. Met. Ceram.* **5**, 981–986 (1966)
 27. K. Kaviyaranan, T. Sivasankar, V.K. Ponnusamy, S. Anandan, Ni-ZnO nanocomposites assembled under various morphologies like columnar, nanochains, and granular structure for removal of pollutants. *Mater. Chem. Phys.* **252**, 123299 (2020)
 28. X. Wang, J. Yang, L. Shi, M. Gao, Surfactant-free synthesis of CuO with controllable morphologies and enhanced photocatalytic property. *Nanoscale Res. Lett.* **11**, 1–7 (2016)
 29. B. Liu, H.C. Zeng, Mesoscale organization of CuO nanoribbons: formation of ‘dandelions’. *J. Am. Chem. Soc.* **126**, 8124–8125 (2004)
 30. S.J. Gregg, K.S. Sing, *Adsorption, Surface Area and Porosity* (Academic Press, London, 1982)
 31. L. Xiao, D. Mei, M. Cao, D. Qu, B. Deng, Effects of structural patterns and degree of crystallinity on the performance of nanostructured ZnO as anode material for lithium-ion batteries. *J. Alloys Compd.* **627**, 455–462 (2015)
 32. G. Li, Y. Li, J. Chen, P. Zhao, D. Li, Y. Dong, L. Zhang, Synthesis and research of egg shell-yolk NiO/C porous composites as lithium-ion battery anode material. *Electrochim. Acta* **245**, 941–948 (2017)
 33. J. Zhang, J. Qiao, K. Sun, Z. Wang, Balancing particle properties for practical lithium-ion batteries. *Particuology* **61**, 18–29 (2022)
 34. Y. Su, M. Wang, M. Zhang, L. Chen, N. Li, L. Chen, Y. Chen, J. Liu, Y. Li, The positive role of the single crystal morphology in improving the electrochemical performance of li-rich cathode materials. *J. Alloys Compd.* **905**, 164204 (2022)
 35. R. Singh, T. Ichikawa, A. Jain, Zinc oxide as promising anode material for li-ion battery, in: *Nanostructured Zinc Oxide* (Elsevier, 2021), pp. 575–603
 36. A.R. Bredar, A.L. Chown, A.R. Burton, B.H. Farnum, Electrochemical impedance spectroscopy of metal oxide electrodes for energy applications. *ACS Appl. Energy Mater.* **3**, 66–98 (2020)
 37. W. Choi, H.-C. Shin, J.M. Kim, J.-Y. Choi, W.-S. Yoon, Modeling and applications of electrochemical impedance

- spectroscopy (EIS) for lithium-ion batteries. *J. Electrochem. Sci. Technol.* **11**, 1–13 (2020)
38. K. Xu, Nonaqueous liquid electrolytes for lithium-based rechargeable batteries. *Chem. Rev.* **104**, 4303–4418 (2004)
39. S. Rastgar, S. Shahrokhian, Nickel hydroxide nanoparticles-reduced graphene oxide nanosheets film: layer-by-layer electrochemical preparation, characterization and rifampicin sensory application. *Talanta* **119**, 156–163 (2014)
40. H. Long, T. Shi, H. Hu, S. Jiang, S. Xi, Z. Tang, Growth of hierarchal mesoporous NiO nanosheets on carbon cloth as binder-free anodes for high-performance flexible lithium-ion batteries. *Sci. Rep.* **4**, 7413 (2014)
41. A. Xiao, S. Zhou, C. Zuo, Y. Zhuan, X. Ding, Synthesis of nickel oxide nanospheres by a facile spray drying method and their application as anode materials for lithium ion batteries. *Mater. Res. Bull.* **70**, 200–203 (2015)
42. H. Zhang, G. Zhang, Z. Li, K. Qu, L. Wang, W. Zeng, Q. Zhang, H. Duan, Ultra-uniform CuO/Cu in nitrogen-doped carbon nanofibers as a stable anode for li-ion batteries. *J. Mater. Chem. A* **4**, 10585–10592 (2016)
43. Z. Deng, Z. Ma, Y. Li, Y. Li, L. Chen, X. Yang, H.-E. Wang, B.-L. Su, Boosting lithium-ion storage capability in CuO nanosheets via synergistic engineering of defects and pores. *Front. Chem.* **6**, 428 (2018)
44. E. Thauer, G. Zakharova, E. Andreikov, V. Adam, S. Wegener, J.-H. Nölke, L. Singer, A. Ottmann, A. Asyuda, M. Zharnikov et al., Novel synthesis and electrochemical investigations of ZnO/C composites for lithium-ion batteries. *J. Mater. Sci.* **56**, 13227–13242 (2021)
45. C. Zhao, J. Fan, J. Guo, X. Zhang, M. Jahanzaib, Z. Zhao, W. Jiang, L. Song, C. Zhao, Dual carbon-supported ZnO/CuO nanocomposites as an anode with improved performance for li-ion batteries. *Energy Fuels* (2022)
46. C.J. Pelliccione, Y. Ding, E.V. Timofeeva, C.U. Segre, In situ XAFS study of the capacity fading mechanisms in ZnO anodes for lithium-ion batteries. *J. Electrochem. Soc.* **162**, A1935 (2015)

Publisher's Note Springer Nature remains neutral with regard to jurisdictional claims in published maps and institutional affiliations.